Journal of Thermal Science Vol.29, No.1 (2020) 144–158

**https://doi.org/10.1007/s11630-019-1167-8** **Article ID: 1003-2169(2020)01-0144-15**

# A High Order Control Volume Finite Element Method for Transient Heat Conduction Analysis of Multilayer Functionally Graded Materials with Mixed Grids

**LIU Qi, MING Pingjian*, ZHAO Haiyang, ZHANG Wenping**

College of power and energy engineering, Harbin Engineering University, Harbin 150001, China



**Abstract:** This paper describes a new two-dimensional (2-D) control volume finite element method (CV-FEM) for transient heat conduction in multilayer functionally graded materials (FGMs). To deal with the mixed-grid problem, 9-node quadrilateral grids and 6-node triangular grids are used. The unknown temperature and material properties are stored at the node. By using quadratic triangular grids and quadratic quadrilateral grids, the present method offers greater geometric flexibility and the potential for higher accuracy than the linear CV-FEM. The properties of the FGMs are described by exponential, quadratic and trigonometric grading functions. Some numerical tests are studied to demonstrate the performance of the developed method. First, the present CV-FEM with mixed high-order girds provides a higher accuracy than the linear CV-FEM based on the same grid size. Second, the material properties defined location is proved to have a significant effect on the accuracy of the numerical results. Third, the present method provides better numerical solutions than the conventional FEM for the FGMs in conjunction with course high-order grids. Finally, the present method is also capable of analysis of transient heat conduction in multilayer FGM.

**Keywords: finite volume method, functionally graded materials, transient heat conduction**

## 1. Introduction

Functionally graded materials (FGMs) are a new class of materials that comprise a spatial gradation in structure and/or composition, designed for a special characteristic for harsh working conditions. The concept of FGMs was first introduced in the early 1980s [1] for aerospace structural applications. However, due to its attractive physical and mechanical properties, FGMs have been applied broadly to various industrial fields in recent years, for example, in machine parts [2–4], biomaterial [5], and electric power equipment [6–8]. The development of instruments for design in FGMs is a challenge for modern manufacturing industry. On this path, analytical and numerical approaches are very useful tools for design and study of FGMs.

Heat conduction and thermoelastic analysis in FGMs have been studied by many investigators using analytical and numerical approaches. Ootao et al. [9] obtained the analytical solutions for the temperature and thermal stress distributions of a hollow cylinder in multilayered composite laminates by applying the methods of Fourier cosine transform and Laplace transform. Using the same analytical method, Ootao et al. also studied the 3-D

Received: Sep 03, 2018 Corresponding author: MING Pingjian E-mail: pingjianming@hrbeu.edu.cn

thermoelastic field of nonhomogeneous hollow cylinder with a moving heat source [10] and nonhomogeneous functionally graded rectangular plate with partial heating [11]. Sankar et al. [12] found exact solution for the 2-D and 3-D thermoelastic problems for functionally graded beam with the thermoelastic constants which vary exponentially through the thickness. Kwon et al. [13] studied the case of a gradient sphere under nonuniform temperature variations by using a numerical integration procedure. Zhou et al. [14] reported the exact analysis for a transient thermal conduction problem of a functionally graded thick strip in contact with fluid. Although the analytical approaches can provide exact solutions of the temperature of the FGMs, they are limited to simple geometries, certain types of material properties, and specific types of boundary conditions [9-14]. As a result, the numerical approach is a better choice to design and investigate these materials. Sladek et al. [15] presented a meshless local boundary integral equation method (LBIED) for 3-D axisymmetric transient heat conduction for exponentially graded materials. Sutradhar et al. [16] extended the Galerkin BEM to 3-D transient heat conduction problem considering exponential material variation with the method of Laplace transform. Sutradhar et al. [17] proposed a "simple" boundary element method (BEM) for steady-state and transient heat conduction analysis in FGMs, which leads to a boundary-only formulation without any domain integral. Wang et al. [18] developed a virtual boundary collocation method (VBCM) and pointed out the advantages and disadvantages for the 2-D transient heat conduction problems in non-homogeneous FGMs. Wang et al. [19] determined the 1-D transient temperature field in FGM plate, shell and sphere by the finite element method together with the finite difference technique (FEM/FD). Yan Yun [20] applied a statistical second-order two-scale (SSOTS) to analyze the heat conduction performances of inconsistent random structures with varying volume fraction distribution of grains and those with varying probability model distribution. Kimand and Paulino [21] developed 8-node quadrilateral graded finite elements using a generalized isoparametric formulation to interpolate the unknown displacement, and the material parameters. The results showed that the FEM with Q8 graded element provided smoother stress profile than that with conventional homogeneous 4-node and 8-node quadrilateral elements. Aboudi et al [22] proposed the higher-order micromechanical theory (HOTFGM) to the FGM to capture the heterogeneous properties of FGM based on two-step volume discretization, because the original formulation of the HOTFGM was computationally intensive, Bansal, Pindera and zhong [23, 24] developed a reformulation of the HOTFGM with rectangular subcells based on the local/global conductivity and stiffness matrices formulations, and the reformulation significantly decreased the computational costs.

In contrast to the numerical methods discussed above, the control volume finite element method (CV-FEM) is also an efficient method for the heat conduction and thermoelastic analysis in FGMs. For 2-D problems, Gong et al. [25] developed a staggered cell vertex finite volume to unsteady thermoelastic problems for orthotropic materials. The material properties were stored at the grid center, which was proved to be suitable for dealing with multi-phase materials and multilayer composites. Gong et al. [26] presented an unstructured finite-volume time-domain method (UFVTDM) based on 4-node quadrilateral (Q4) grid and 3-node triangular (T3) grid to transient heat conduction problem in multilayer FGMs. Charoensuk and Vessakosol [27] applied the CV-FEM based on a 6-node triangular grid to transient heat conduction problems for exponentially graded materials. The results showed that the quadratic CV-FEM provided better numerical precision than the linear CV-FEM under the same grid size. The paper also compared the numerical results based on the CV-FEM and conventional FEM for 6-node triangular grids, and it pointed out that the CV-FEM provided more accurate than the conventional FEM. However, the developed high order CV-FEM was only capable of 6-node triangular grids and exponentially FGMs.

6-node triangular grids offer greater flexibility in describing bodies having curved boundary geometrics and also have the potential for enhanced accuracy due to the nature of quadratic interpolation [27]. The purpose of this paper is to present a reliable numerical method for 2-D heat conduction problems based on 9-node quadrilateral grid (Q9) and 6-node triangular grid (T6) with different kinds of functional material variation. The unknown temperature and material properties were stored at the grid node. Some numerical problems were studied to demonstrate the efficient of the proposed method. The remainder of this paper is organized as follow.

In Section 2, the governing equation for the 2D transient heat conduction is given. In Section 3, the quadratic CV-FEM for spatial discretization and a fully implicit scheme for time discretization of governing equation are presented. In Section 4, some test cases are provided to verify the present method. Finally, a brief conclusion is given in section 5.

## 2. Mathematic Model

### 2.1 Governing equations

The governing equation for the transient heat conduction with no consideration of internal heat sources is given by

$$\frac{\partial}{\partial x}\left(k_x\frac{\partial T}{\partial x}\right)+\frac{\partial}{\partial y}\left(k_y\frac{\partial T}{\partial y}\right)=\rho c\frac{\partial T}{\partial t} \tag{1}$$

where $T=T(x, y, t)$ is the temperature field. $k_x$ and $k_y$ are the thermal conductivities in the $x$ direction and $y$ direction respectively. $\rho$ is the density and $c$ is the specific heat. The thermal conductivities $k$, specific heat $c$ and density $\rho$ are defined by a function of space coordinates in this paper. The initial condition for the solution domain at time $t=0$ is assumed as

$$T(x,y)\big|_{t=0}=T_{\text{int}} \tag{2}$$

where $T_{\text{int}}$ is the initial temperature. Three types of boundary conditions are considered. For the Dirichlet boundary $l_D$, the temperature $T_B$ on the boundary is given

$$T=T_B \text{ on } l_D \tag{3}$$

For the Neumann boundary $l_N$

$$-k_x\frac{\partial T}{\partial x}n_x-k_y\frac{\partial T}{\partial y}n_y=q_B \text{ on } l_N \tag{4}$$

where $q_B$ is the fixed normal heat flux on the boundary $l_N$. $n_x$ and $n_y$ are the components of the outward unit vector $\boldsymbol{n}$ in $x$ and $y$ directions.

For the Robin boundary $l_R$

$$k_x\frac{\partial T}{\partial x}+k_y\frac{\partial T}{\partial y}=-h_B\left(T-T_\infty\right) \text{ on } l_R \tag{5}$$

where $h_B$ is the heat convective coefficient and $T_\infty$ is environment temperature on the boundary $l_R$.

### 2.2 Discretization of solution domain

In this section, the detailed numerical discretization process of Eq. (1) based on 6-node triangular grid and 9-node quadrilateral grid is given. An arbitrary 2D computational domain can be meshed with T3 and Q4 grids or with T6 and Q9 grids. For example, connect the grid centers and the mid-point of grid edges, a typical control volume around vertex $N_1$ is constructed (see Fig. 1(a)). Fig. 1(b) illustrates three different effective control volumes within T6 and Q9 grids. The way to construct a control volume within T6 and Q9 grids is similar as the way within T3 and Q4 grids. Connecting the centers of each smaller triangles $T_1$, $T_2$, $T_3$, and $T_4$ or quadrangles

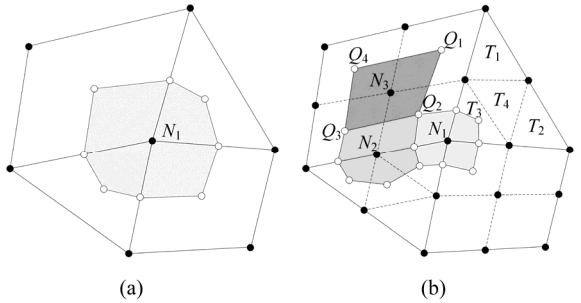


**Fig. 1** The scheme of control volume with (a) linear mixed grids, (b) quadratic mixed grids

$Q_1$, $Q_2$, $Q_3$ and $Q_4$, and the mid-point of its edges, three typical control volumes are constructed around node $N_1$, $N_2$, and $N_3$ as shown in Fig. 1(b). For any control volume around node $N_1$ in Fig. 1(b), the integral of Eq. (1) can be written as

$$\int_S\left[\frac{\partial}{\partial x}\left(k_x\frac{\partial T}{\partial x}\right)+\frac{\partial}{\partial y}\left(k_y\frac{\partial T}{\partial y}\right)\right]dS=\int_S\left(\rho c\frac{\partial T}{\partial t}\right)dS \tag{6}$$

Appling the Gaussian quadrature formula, the LHS of Eq. (6) can be written as

$$\begin{aligned}&\int_S\left[\frac{\partial}{\partial x}\left(k_x\frac{\partial T}{\partial x}\right)+\frac{\partial}{\partial y}\left(k_y\frac{\partial T}{\partial y}\right)\right]dS\\&=\sum_{i=1}^{nk3}\int_{l_i}\left[k_x\frac{\partial T}{\partial x}n_x+k_y\frac{\partial T}{\partial y}n_y\right]dl\\&+\sum_{i=1}^{nk4}\int_{l_i}\left[k_x\frac{\partial T}{\partial x}n_x+k_y\frac{\partial T}{\partial y}n_y\right]dl\\&=\sum_{i=1}^{nk3}\left[\int_{l_i}k_x\frac{\partial T}{\partial x}n_x dl+\int_{l_i}k_y\frac{\partial T}{\partial y}n_y dl\right]\\&+\sum_{i=1}^{nk4}\left[\int_{l_i}k_x\frac{\partial T}{\partial x}n_x dl+\int_{l_i}k_y\frac{\partial T}{\partial y}n_y dl\right]\\&=\sum_{i=1}^{nk3}\int_{l_i}k_\alpha\frac{\partial T}{\partial \alpha}n_\alpha dl+\sum_{i=1}^{nk4}\int_{l_i}k_\alpha\frac{\partial T}{\partial \alpha}n_\alpha dl\end{aligned} \tag{7}$$

where $\alpha\in\{x,y\}$; $nk3$ and $nk4$ are the numbers of the T6 grids and Q9 grids around node $N_1$, respectively. $l_i$ is the path of integration in the $i$th grid. According to the knowledge of shape function [28], the temperature and material properties at any point in a grid can be interpolated using the following equations

$$T=\sum_{i=1}^{ns}N_iT_i,\ \rho=\sum_{i=1}^{ns}N_i\rho_i,\ c=\sum_{i=1}^{ns}N_ic_i,\ k=\sum_{i=1}^{ns}N_ik_i \tag{8}$$

where $ns$ is the sum of the number of nodes in a grid, for T6, $ns=6$ grid, and for Q9 grid, $ns=9$. $N_i$ is the shape function of the $i$th node; $T_i$, $\rho_i$, $c_i$ and $k_i$ are the temperature, density, specific heat and thermal conductivities at the $i$th node, respectively. The present method is developed for multilayer FGMs. In order to describe the variation of the material properties at the interface between different layers more accuracy, the material properties of the nodes at the interface are calculated twice using the given grading function and then stored. The derivatives of temperature in each grid can be given by

$$\frac{\partial T}{\partial \alpha}=\sum_{i=1}^{ns}\frac{\partial N_i}{\partial \alpha}T_i \tag{9}$$

Substituting Eq. (9) into Eq. (7), then the problem comes down to

$$\int_l k_\alpha\sum_{i=1}^{ns}\frac{\partial N_i}{\partial \alpha}T_i n_\alpha dl=\sum_{i=1}^{ns}T_i\int_l k_\alpha\frac{\partial N_i}{\partial \alpha}n_\alpha dl \tag{10}$$

The solution procedure of the derivatives of shape functions and its integral are given in detail in Appendix 1. The RHS of Eq. (6) is discretized using the backward difference scheme as

$$\int_S \left( \rho c \frac{\partial T}{\partial t} \right) dS = \rho c S \frac{T^t - T^{t-\Delta t}}{\Delta t} \tag{11}$$

where $S$ is the area of the control volume. $\Delta t$ is the size of time step. $T^t$ is the unknown temperature at the current time $t$, and $T^{t-\Delta t}$ is the known temperature at the last time step $t-\Delta t$.

Imposing the Neumann and Robin boundary conditions on the integral form of Eq. (1), it becomes

$$\begin{aligned} &\int_{l_{in}} \left( k_x \frac{\partial T}{\partial x} n_x + k_y \frac{\partial T}{\partial y} n_y \right) dl - \int_{l_N} q_B dl \\ &- \int_{l_R} h_B \left( T - T_\infty \right) dl \\ &= \rho c S \frac{T^t - T^{t-\Delta t}}{\Delta t} \end{aligned} \tag{12}$$

where $l_{in}$ is an internal surface of the control volume.

## 3. Numerical Examples

In this section, six numerical tests have been studied to demonstrate the accuracy and capability of the developed CV-FEM.

### 3.1 Homogeneous material problems

#### 3.1.1 Assessment on predictive quality of the present method

The first test case is a homogeneous rectangular plate with non-uniform heating on three planes (see Fig. 2). The dimension of the homogeneous rectangular plate is 5 m × 10 m. The thermal conductivity $k$ of material is 1 W/(m·K). The boundary conditions are

$$\begin{aligned} &T(x,10) = 100\sin(\pi x/10) \\ &T(0,y) = T(x,0) = 0 \\ &q(5,\mathrm{y}) = 0 \end{aligned} \tag{13}$$

The exact temperature in the computational domain is

$$T(x,y) = 100 \frac{\sinh(\pi y/10)\sin(\pi x/10)}{\sinh(\pi)} \tag{14}$$

To assess the accuracy of the linear and quadratic CV-FEM with mixed grids, three meshes are introduced (see Fig. 3). Table 1 lists the temperature distributions at different locations with Mesh 1 and Mesh 2. The compared results show that the high-order CV-FEM could provide better numerical precision than the first-order CV-FEM under the same number of degrees of freedom. By increasing the order of interpolation function, the computational precision can be improved greatly just as the same way as refining the grid. Table 2 lists the temperature at the different locations with Mesh 2 and Mesh 3 based on the quadratic CV-FEM. The results also agree well with the exact solution, and Mesh 2 is supposed to be fine enough for this problem.

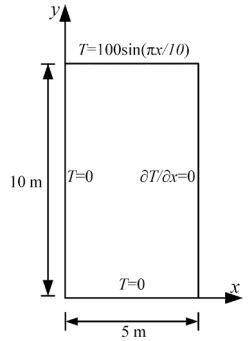


**Fig. 2** The computational domain and boundary conditions

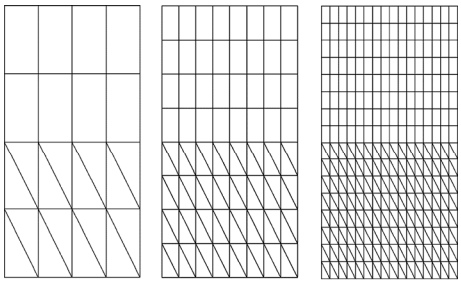


**Fig. 3** The computational meshes of the rectangular plate

**Table 1** Comparison of the temperatures inside the computational domain at different locations

| $y$ | $x$ | Exact $T$/°C | CV-FEM (Order=1) Mesh 2 (T3+Q4) | | CV-FEM (Order=2) Mesh 1 (T6+Q9) | |
|---|---|---|---|---|---|---|
| | | | $T$/°C | Error/% | $T$/°C | Error/% |
| 2.5 | 1.25 | 2.878 46 | 2.851 66 | 0.931 1 | 2.896 03 | 0.610 3 |
| | 2.5 | 5.318 7 | 5.269 18 | 0.931 1 | 5.350 11 | 0.590 6 |
| | 3.75 | 6.949 22 | 6.884 52 | 0.931 1 | 6.987 25 | 0.547 3 |
| 5 | 1.25 | 7.625 67 | 7.524 11 | 1.331 9 | 7.690 92 | 0.855 6 |
| | 2.5 | 14.090 4 | 13.902 7 | 1.331 9 | 14.205 8 | 0.818 6 |
| | 3.75 | 18.41 | 18.164 8 | 1.331 9 | 18.555 6 | 0.791 |

**Table 2** Comparison of the temperatures inside the computational domain at different locations based on quadratic CV-FEM with Mesh 2 and Mesh 3

| $y$ | $x$ | Exact $T$/°C | CV-FEM (Order=2) Mesh 2 (T6+Q9) | | CV-FEM (Order=2) Mesh 3 (T6+Q9) | |
|---|---|---|---|---|---|---|
| | | | $T$/°C | Error/% | $T$/°C | Error/% |
| 2.5 | 1.25 | 2.878 46 | 2.882 89 | 0.153 9 | 2.879 58 | 0.038 91 |
| | 2.5 | 5.318 7 | 5.326 57 | 0.147 9 | 5.320 68 | 0.037 22 |
| | 3.75 | 6.949 22 | 6.958 78 | 0.137 5 | 6.951 63 | 0.034 68 |
| 5 | 1.25 | 7.625 67 | 7.641 42 | 0.206 5 | 7.629 56 | 0.051 01 |
| | 2.5 | 14.090 4 | 14.118 1 | 0.196 5 | 14.097 2 | 0.048 26 |
| | 3.75 | 18.41 | 18.444 8 | 0.189 | 18.418 6 | 0.046 71 |

### 3.1.2 Assessment on application for different types of grids for transient heat conduction problem

To further evaluate the application of the developed CV-FEM for different types of grids for transient heat conduction problem, a homogeneous unit square strip subjected to uniformed heat flux condition is analyzed (see Fig. 4). The material properties are as follow: $k$=1 W/m·K and $\alpha$=1 m$^2$/s. The time step $\Delta t$=0.004 s. The boundary conditions are

$$\begin{aligned} &T(0,\mathrm{y})=0 \\ &q(x,0)=1000 \\ &q(100,y)=q(x,100)=0 \end{aligned} \tag{15}$$

Three types of meshes are chosen for this study. Contour plots of the temperature at time $t$=2 s for different grids are plotted in Fig. 5. From the comparisons of isothermal with those obtained from the linear cell vertex finite volume method [26], good numerical solutions can be obtained by the present method with coarse quadrilateral grids or triangular grids and mixed grids. The temperature at the position (100, 0) and (100, 50) are plotted against time and compared with the solutions from the MWLS [29] and MLPG [30] (see Fig. 6 and Fig. 7). The results also show excellent agreement.

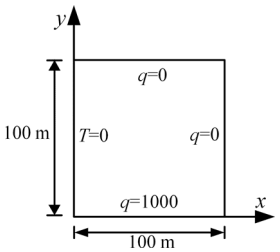


**Fig. 4** The geometry and boundary conditions

### 3.1.3 Aircraft engine compressor

To illustrate the accuracy and capability of the present CV-FEM to irregular areas, the steady heat conduction in an aircraft engine compressor in Ref. [32] is studied, and the geometry and boundary conditions are given in Fig. 8. The inner surface (boundary segment B-C) of the compressor is fixed at the temperature $T$=1000°C; the boundary segment A-B and C-D are insulated, and the other surfaces are subjected to uniformed convective boundary condition, with the environment $h$=10 W/(m$^2$·K), $u_\infty$=300°C. The thermal conductivity $k$=20 W/(m·K). The CV-FEM mesh employed 1093 high-order mixed grids is shown in Fig. 9(a). Here the solution of the problem is compared with the commercial FEM software ANSYS with 1023 8-noded plane grids (quadratic) as shown in Fig. 9(b).

The temperature of the compressor along $y$=0 are plotted and compared with the results from FEM in Fig. 10. It can be observed that the results predicted by the developed CV-FEM are in good agreement with the ANSYS solutions. Fig. 11 plots the overall temperature distribution in the aircraft engine compressor.

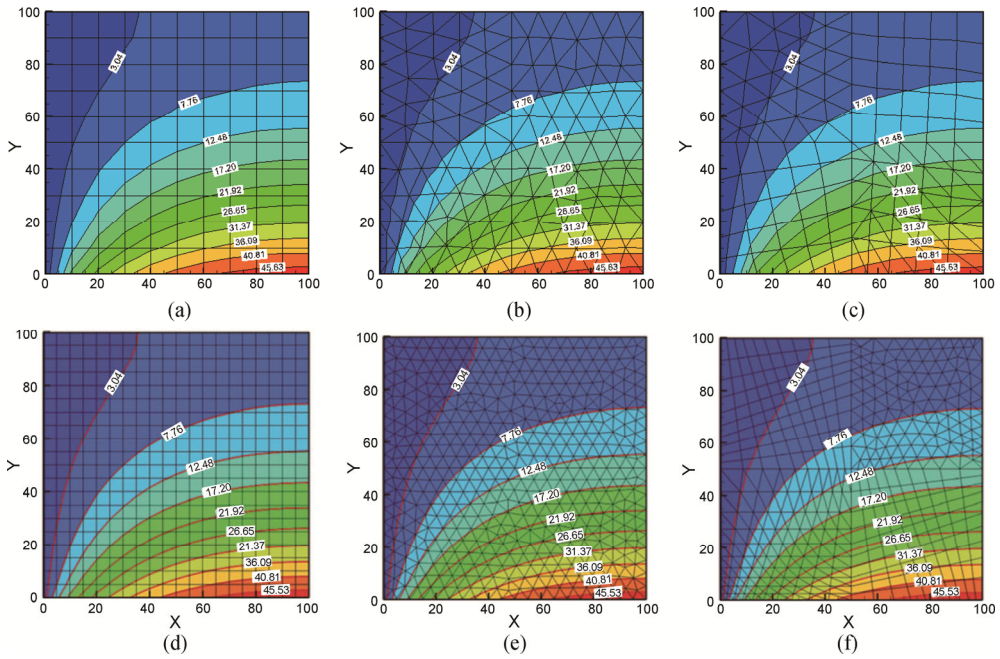


**Fig. 5** Contours of temperature at $t$=2 s: (a) results with 100 quadrilateral grids (quadratic); (b) results with 224 triangular grids (quadratic); (c) results with 154 mixed grids (quadratic); (d) results with 400 quadrilateral grids (linear) in [26]; (e) results with 896 triangular grids (linear) in [26]; (f) results with 628 mixed grids (linear) in [26]

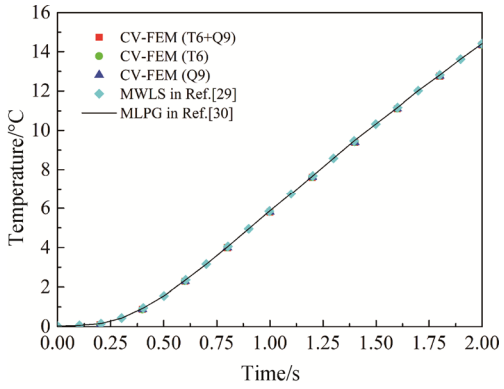


**Fig. 6** The temperature distributions at different time at (100,0)

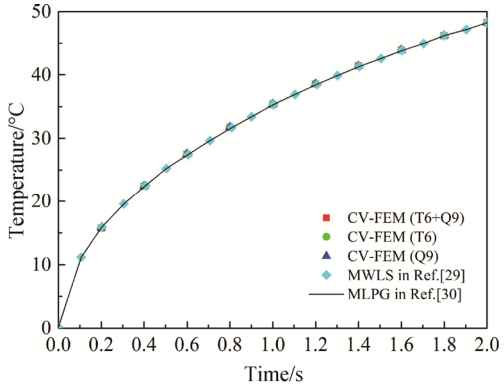


**Fig. 7** The temperature distributions at different time at (100,50)

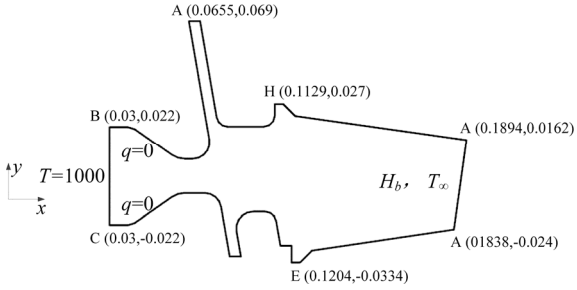


**Fig. 8** The geometry and boundary conditions

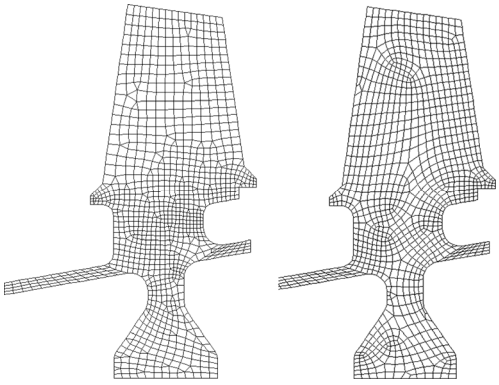

**Fig. 9** (a) The CV-FEM mesh with 1093 mixed grids, (b) The FEM mesh with 1023 8-node plane grids

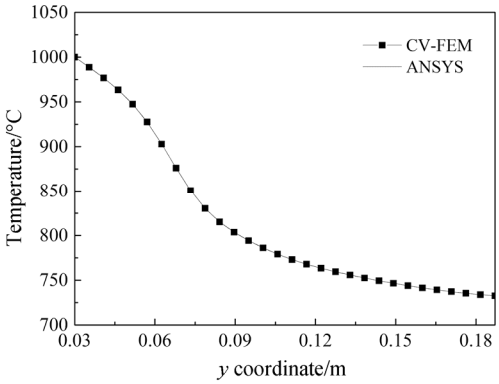


**Fig. 10** The temperature distributions along $y$=0 for aircraft engine compressor

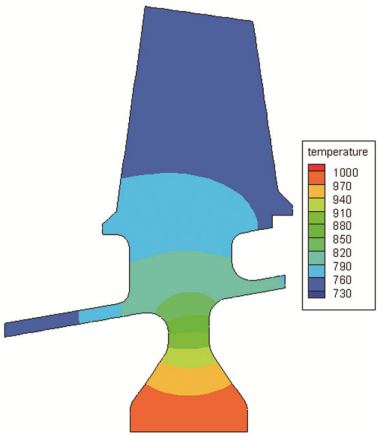


**Fig. 11** Contours of temperature of the aircraft engine compressor

### 3.2 FGMs problems

#### 3.2.1 Unit square strip with three kinds of material variation

In this section, in order to validate the effectiveness of the proposed method for functionally graded materials, a unit square in Fig. 12(a) with three different types of materials variation is studied. Two meshes are introduced for this case (see Fig. 12(b) and (c)). The boundary conditions are

$$\begin{aligned} &T(x,1)=100\\ &T(x,0)=0\\ &q(1,y)=q(0,y)=0 \end{aligned} \tag{16}$$

**Exponential material gradation**

In analyzing the thermoelastic problems in FGMs, the properties of FGMs described by grading functions can be either defined at the grid centroid [26] or at the grid node [27]. In the present study, it is found that the material properties defined location have a significant effect on the numerical accuracy, especially in the analysis of highly graded material. To demonstrate this, a

square strip heat conduction problem is introduced. The thermal conductivity of the material is defined as

$$k(x,y)=k(y)=5\mathrm{e}^{2\beta y} \tag{17}$$

The analytical solution for the temperature field is

$$T(x,y)=T\frac{1-\mathrm{e}^{-2\beta y}}{1-\mathrm{e}^{-2\beta L}} \tag{18}$$

where $T$=100，$L$=1, various values of $\beta$=0, 0.5, 0.75, 1, 1.25, 1.5 are considered in this study.

Fig. 13(a) and 13(b) show the temperature variation along $x$=0.5 for different material defined locations for various values of $\beta$ based on Mesh 1. As can be seen from Fig. 13(a), there are some significant errors at the mid-points (node1, node2 node3 and node4) of the grid edges, and the errors increase significantly when the value of $\beta$ increasing. While compared to the solutions with material properties defined at the grid centroid, the solutions with material properties defined at the grid node are in excellent agreement with those from analytical solutions (see Fig. 13(b)). Table 3 and Table 4 list the comparison results based on different material properties defined locations for $\beta$=1 and $\beta$=1.5. The results indicate that the CV-FEM with material properties storied at the grid centroid is not suitable to solve the heat conduction problem with highly graded material especially in combination with coarse mesh. The results from CV-FEM at $\beta$=0.5 and $\beta$=1.5 are also compared with those obtained by conventional FEM based on Mesh 2, see Table 5. The results show that the CV-FEM provides more accurate solution than the conventional EFM.

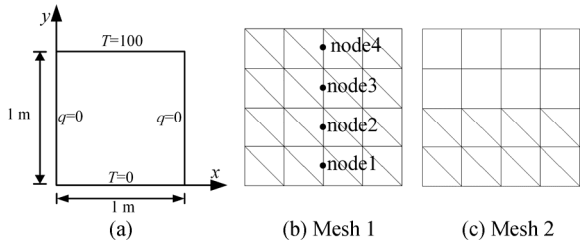


**Fig. 12** (a) Geometry and boundary conditions of the FGM strip problem, (b) triangular grids and (c) mixed grids

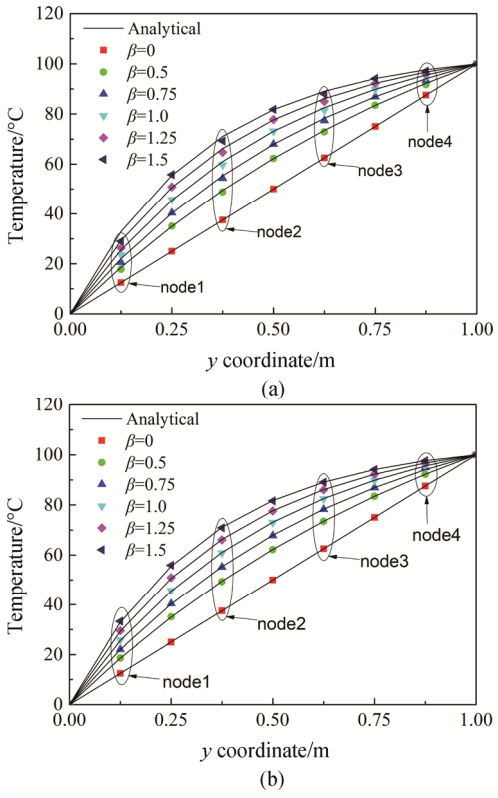


**Fig. 13** The temperature distributions along $x$=0.5 with different values of $\beta$: (a) material properties defined at the cell center and (b) material properties defined at the node

### Parabolic and trigonometric material gradation

Next, the FGM strip transient heat conduction problem with other two different material properties are considered. The same geometry and boundary conditions in Fig. 12(a) are adopted in this analysis. Initial

**Table 3** Comparison of the temperatures with different material defined locations for $\beta$=1

| $x$ | $\beta$=1 | | | | |
|---|---|---|---|---|---|
| | Exact $T$/°C | material properties defined at the grid centroid | Error /% | material properties defined at the grid node | Error /% |
| 0.125 | 25.582 | 23.417 4 | 8.461 4 | 25.762 | 0.703 6 |
| 0.25 | 45.505 4 | 45.694 6 | 0.415 8 | 45.702 4 | 0.432 9 |
| 0.375 | 61.021 7 | 59.740 2 | 2.100 1 | 60.809 4 | 0.347 9 |
| 0.5 | 73.105 8 | 73.175 4 | 0.095 2 | 72.977 | 0.176 2 |
| 0.625 | 82.516 9 | 81.472 6 | 1.265 6 | 82.449 2 | 0.082 0 |
| 0.75 | 89.846 3 | 89.843 8 | 0.002 8 | 89.804 6 | 0.046 4 |
| 0.875 | 95.554 5 | 94.921 1 | 0.662 9 | 95.541 9 | 0.013 2 |

**Table 4** Comparison of the temperatures with different material defined locations for $\beta$=1.5

| $x$ | $\beta$=1.5 | | | | |
|---|---|---|---|---|---|
| | Exact $T$/°C | material properties defined at the grid centroid | Error /% | material properties defined at the grid node | Error /% |
| 0.125 | 32.909 5 | 28.963 7 | 11.99 | 33.301 3 | 1.190 4 |
| 0.25 | 55.527 9 | 55.820 6 | 0.527 1 | 55.905 0 | 0.679 1 |
| 0.375 | 71.073 2 | 69.259 45 | 2.552 1 | 70.853 7 | 0.308 9 |
| 0.5 | 81.757 4 | 81.835 9 | 0.096 0 | 81.625 0 | 0.162 0 |
| 0.625 | 89.100 5 | 87.945 6 | 1.296 2 | 89.049 8 | 0.057 0 |
| 0.75 | 94.147 4 | 94.143 4 | 0.004 2 | 94.111 7 | 0.037 9 |
| 0.875 | 97.616 04 | 97.070 9 | 0.558 5 | 97.611 81 | 0.004 3 |

**Table 5** Comparison of the temperatures at different locations based on CV-FEM and FEM

| $\beta$ | $x$ | Exact $T$/°C | FEM (T6+Q9) | | CV-FEM (T6+Q9) | |
|---|---|---|---|---|---|---|
| | | | $T_{FEM}$/°C | Error/% | $T_{FVM}$/°C | Error/% |
| 0.5 | 0.125 | 18.588 7 | 17.765 | 4.431 187 | 18.646 | 0.308 252 |
| | 0.375 | 49.470 1 | 48.845 | 1.263 592 | 49.338 83 | 0.265 352 |
| | 0.625 | 73.520 56 | 72.874 | 0.879 427 | 73.468 2 | 0.071 218 |
| | 0.875 | 92.251 07 | 91.731 | 0.563 755 | 92.237 8 | 0.014 385 |
| 1.5 | 0.125 | 32.909 54 | 29 | 11.879 66 | 33.301 3 | 1.190 415 |
| | 0.375 | 71.073 28 | 69.296 | 2.500 63 | 70.853 7 | 0.308 949 |
| | 0.625 | 89.100 55 | 87.982 | 1.255 379 | 89.049 8 | 0.056 958 |
| | 0.875 | 97.616 04 | 97.067 | 0.562 449 | 97.611 81 | 0.004 333 |

temperature of the strip is zero. Two meshes are introduced (See Fig. 12(b) and 12(c)), and the uniform time step $\Delta t$=0.001 s.

For the quadratic variation of the material properties:

$$k(x,y)=k(y)=5(1+2y)^2 \tag{19}$$

$$c(x,y)=c(y)=(1+2y)^2 \tag{20}$$

For the trigonometric variation of the material properties:

$$k(x,y)=k(y)=5\left(\cos(0.2y)+2\sin(0.2y)\right)^2 \tag{21}$$

$$c(x,y)=c(y)=\left(\cos(0.2y)+2\sin(0.2y)\right)^2 \tag{22}$$

Fig. 14 and Fig. 15 show the temperature distributions with time along $x$=0.5 for the quadratic and trigonometric variations of the material properties based on triangular and mixed grids. A good agreement of both materials can be observed.

### 3.2.2 FGMs thick-wall cylinder with infinite length

As the second example of FGMs, a thick-wall cylinder in FGMs from Ref. [27] is considered, the geometry, boundary conditions and the mesh are depicted in Fig. 16(a) and Fig. 16(b). The mesh consists of 130 triangular and 154 quadrangular quadratic grids, which further assess the application of the present CV-FEM for mixed grids. The inner boundary of the cylinder is prescribed with $T$=0; the outer boundary is described with the Heaviside step function of time variation $T=\overline{T}\cdot H(t)$ with $\overline{T}$=1, and the other two surfaces are insulated. Only one-fourth of the cylinder is considered due to the symmetry of geometry and boundary conditions. The initially temperature of the cylinder is zero, and uniform time step $\Delta t$=0.05 s.

The thermal conductivity and the specific heat are as follow:

$$k=17e^{\lambda(r-r_{in})} \tag{23}$$

$$\alpha=\frac{k}{\rho c}=0.0017e^{\lambda(r-r_{in})} \tag{24}$$

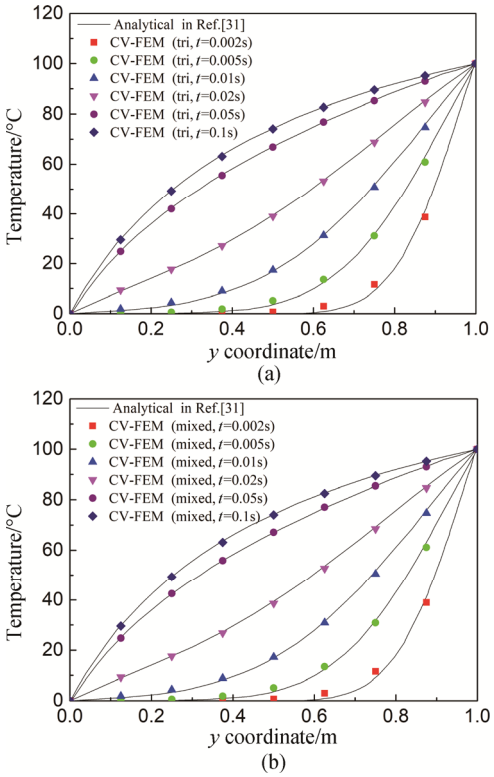


**Fig. 14** Variation of temperature along $x$=0.5 at different times with quadratic material variation: (a) results with triangular grids and (b) results with mixed grids

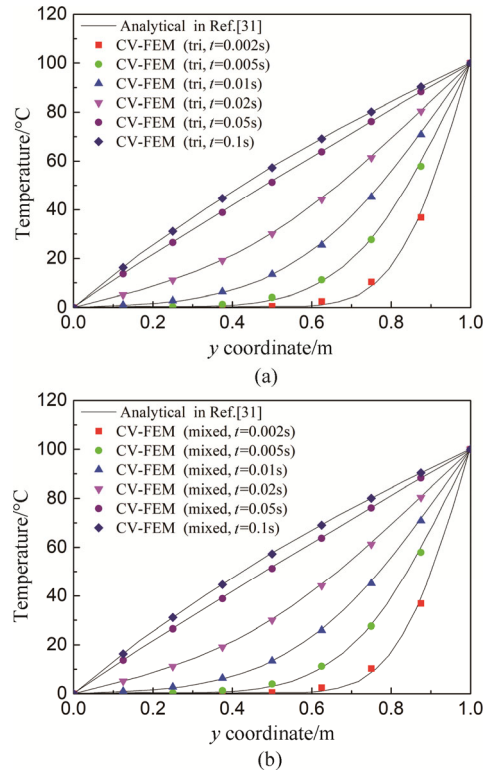


**Fig. 15** Variation of temperature along $x$=0.5 at different times with trigonometric material variation: (a) results with triangular grids and (b) results with mixed grids

Different values of $\lambda$=0, 20 and 50 m$^{-1}$ are used in the analysis. The special case with $\lambda$=0 is studied first. The temperatures at $r$=0.083 3, 0.9, 0.096 7 are plotted against time in Fig. 17. A good agreement for the present method can be observed. It can be seen that the steady state is reached after $t$=15 s. Fig. 18 shows the variation of temperature in the radial direction with various values of $\lambda$ at time $t$=20 s, the results obtained from the developed CV-FEM also match well with the solutions from Ref. [27].

### 3.2.3 FGMs rectangular strip subject to nonuniform convective boundary

To assess the accuracy of the present method in the problem considering Robin boundary, the third problem of FGMs is a rectangular strip [30] under non-uniform convective boundary. The geometry and boundary conditions are depicted in Fig. 19. The domain is meshed using 300 uniform quadratic, quadrilateral grids. The strip is assumed to be heated from the lower surface by ambient media with convective heat-transfer coefficient $h_a$ at $T_\infty(x)=T_a f_a(x)$. The left and right surfaces of the strip are prescribed the temperature $T$=0. The initially temperature of the strip is zero and the time step $\Delta t$=0.005 s. The rest of the numerical parameters are presented as follow:

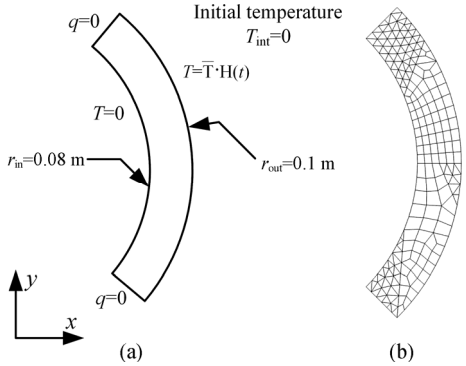


**Fig. 16** (a) Geometry of the third problem and boundary conditions for the FGMs thick-wall cylinder, (b) mixed grids

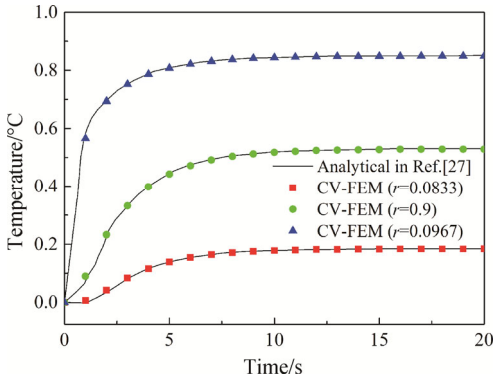


**Fig. 17** Variation of temperature at different time at three radical positions for the FGMs thick-wall cylinder

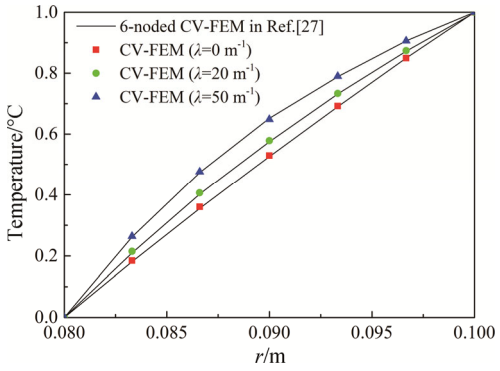


**Fig. 18** Temperature distributions along the radial direction at $t$=20 s for the FGMs thick-wall cylinder

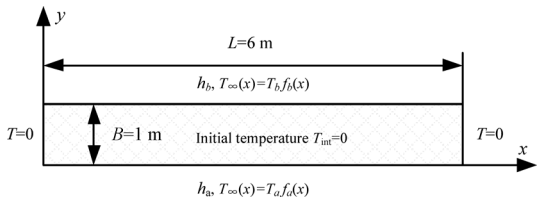


**Fig. 19** Geometry of and boundary conditions for the FGMs rectangular strip

$$T_a=1, T_b=0, h_a=1, h_b=e^{\lambda} \tag{25}$$

$$f_a=\begin{cases}1-(x-3)^2 & 2\le x\le 4\\ 0 & x\le 2, x\ge 4\end{cases} \tag{26}$$

The material properties vary exponential according to

$$k=e^{\lambda y} \tag{27}$$

$$\alpha=\frac{k}{\rho c}=e^{\lambda y} \tag{28}$$

Three different exponential parameters $\lambda$=0, 1 and -1 m$^{-1}$ are studied in numerical calculation. Fig. 20 plots the temperature distributions along the thickness direction at $x$=3 m when $t$=0.1 s and $t$=1 s. The numerical results from the present CV-FEM match well with the MLPG solutions [30].

### 3.3 Multilayer structure

As the last example, a three-layer cylinder structure in traditional composites or FGMs subjected to convective boundary condition is designed in Fig. 21(a). Because of the symmetry, only one-fourth of the annulus cross-section is studied. The initially temperature field is zero. The cylinder is heated from the outer and inner surfaces by ambient media with the temperature at $T_a f_a(r)$ and $T_b f_b(r)$, respectively.

The CV-FEM mesh employed 200 quadratic triangular grids and 200 quadratic quadrilateral grids as shown in Fig. 21(b). Here the CV-FEM results are verified by the FEM solutions obtained from the commercial FEM

software ANSYS. The mesh used in FEM consists of 300 8-noded plane grids (quadratic) as shown in Fig. 21(c). A uniformed time step $\Delta t$=0.005 s is used in the analysis.

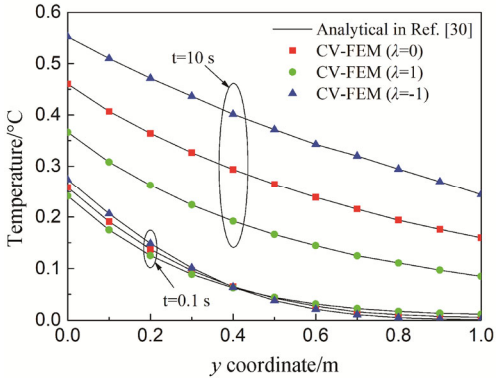


**Fig. 20** Temperature distributions along the thickness direction ($x$=3 m) at $t$=0.1 s and $t$=1 s

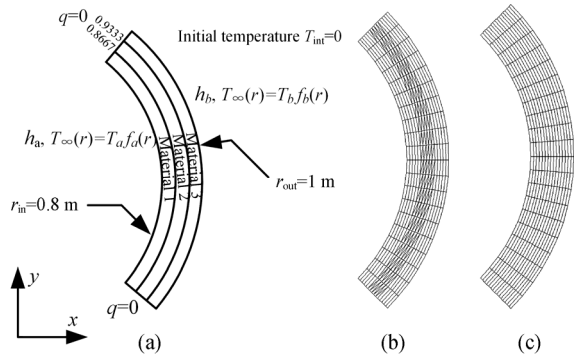


**Fig. 21** (a) Geometry and boundary conditions (b) The CV-FEM mesh with 400 mixed grids and (c) The FEM mesh with 300 8-node plane grids

To analyze the multilayer structure with traditional composite material, the following thermal conductivity and heat specific are used

$$\begin{cases} k=1,\ \alpha=0.1 \text{ when } 0.8\le r\le 0.8667 \\ k=3,\ \alpha=0.4 \text{ when } 0.8667\le r\le 0.9333 \\ k=4,\ \alpha=0.5 \text{ when } 0.9333\le r\le 1 \end{cases} \tag{29}$$

The numerical parameters used for analyzing composite material are given as:

$$h_b=4,\ h_a=1,\ T_b=1,\ T_a=0,\ f_a=f_b=1 \tag{30}$$

For the analysis of multilayer structure with FGMs, the thermal conductivity and heat specific are defined as:

$$\begin{cases} k=k_0\left(\cos(0.2r)+2\sin(0.2r)\right), \\ \alpha=\alpha_0\left(\cos(0.2r)+2\sin(0.2r)\right) \text{ when } 0.8\le r\le 0.8667 \\ k=k_0\left(1+2r\right)^2, \\ \alpha=\alpha_0\left(1+2r\right)^2 \text{ when } 0.8667\le r\le 0.9333 \\ k=k_0\,e^{2\beta r},\ \alpha=\alpha_0 e^{2\beta r} \text{ when } 0.9333\le r\le 1 \end{cases} \tag{31}$$

where $k_0$=1.0 $a_0$=0.01 and $\beta$=1.5. The thermal conductivity variation along the radial direction of the FGMs cylinder is plotted in Fig. 22.

The numerical parameters used for analyzing FGMs are:

$$f_b=\begin{cases} 1-\left(\dfrac{8}{\pi}\theta\right)^2 & -\dfrac{\pi}{8}\le\theta\le\dfrac{\pi}{8} \\ 0 & x\le-\dfrac{\pi}{8}, x\ge\dfrac{\pi}{8} \end{cases} \tag{32}$$

$$h_b=e^{\lambda},\ h_a=1,\ T_a=0,\ T_b=1 \tag{33}$$

where the exponential parameter $\lambda$=2 is used in the analysis.

The temperature of the composite and FGMs cylinders at different locations are plotted and compared with the FEM solutions at four time levels in Fig. 23 and Fig. 24. Fig. 25 plots the comparison of the CV-FEM and FEM solutions along the outer surface of the FGM cylinder at six different time instant. Contours of temperature of the FGM cylinder at five time levels are plotted in Fig. 26. All the numerical solutions obtained with the presented method and the FEM are in good agreement. This test case demonstrates that the present CV-FEM can be successfully used in the application of transient heat conduction problems in multilayer structure with tradition composite materials or FGMs subjected to convective boundary.

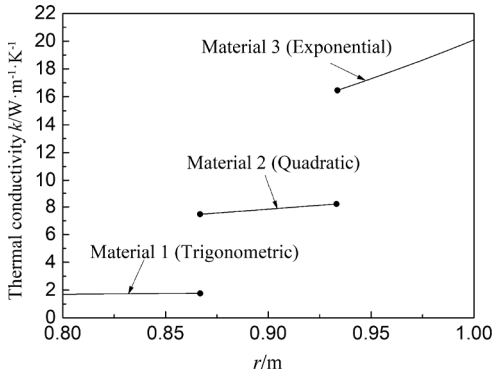


**Fig. 22** Profile of the thermal conductivity $k(r)$ along the radial direction

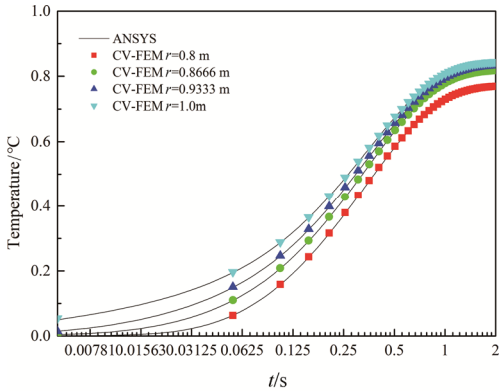


**Fig. 23** Temperature histories at three radical positions for the composite cylinder

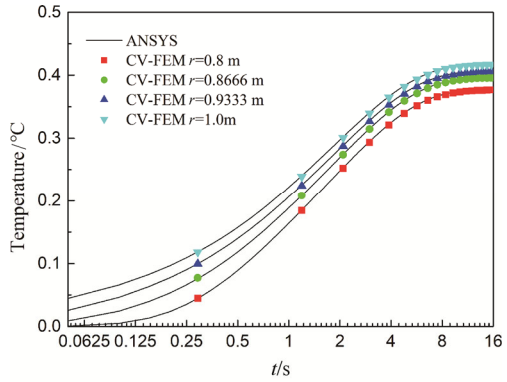


**Fig. 24** Temperature histories at three radical positions for the FGM cylinder

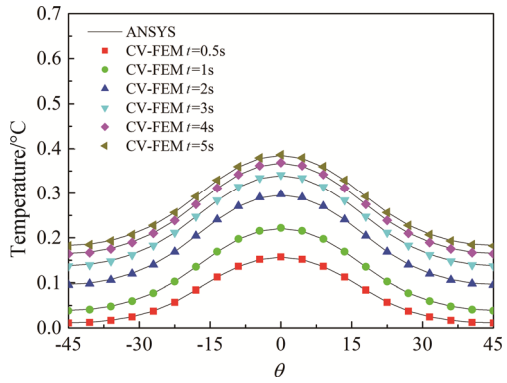


**Fig. 25** Temperature variations at different time levels on the outer surface of the FGM cylinder

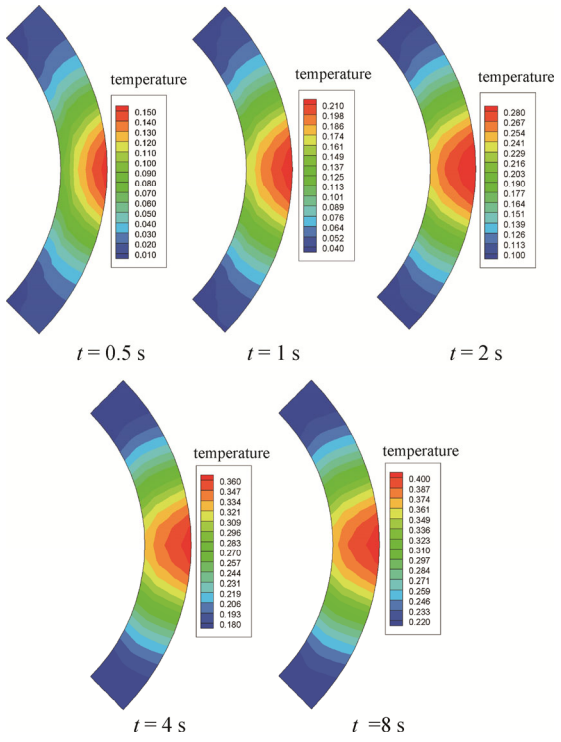


**Fig. 26** Contours of temperature of the FGM cylinder at five time instants

## 4. Conclusions

A high order CV-FEM based on quadratic elements (six-node element and nine-node element) is proposed to analyze heat conduction problems in multilayer FGMs. In the high order CV-FEM, quadratic elements are used to discretize the computational domain, which provides more potential for enhanced geometric flexibility and numerical precision than the linear CV-FEM with original linear element. Three kinds of FGMs with properties described by quadratic, exponential and trigonometric grading functions are analyzed in the solution of problem.

As demonstrated in the numerical solutions with homogeneous material, FGMs or multilayer FGMs, the developed CV-FEM performs well with the steady and transient heat conduction analysis. Compared to the linear CV-FEM and quadratic CV-FEM, the high-order CV-FEM possesses higher precision than the linear CV-FEM for the problem under the same mesh size. In addition, when CV-FEM is used to solve the heat conduction problem in highly graded material, the material properties defined at the grid centroid will cause significant numerical errors at the mid-point of the grid edges, especially in combination with coarse mesh. The numerical solutions with CV-FEM and conventional FEM based on quadratic mixed grids also show that the present method provides more accuracy numerical solution than the counterpart. The present method is adaptable to unstructured high-order mixed grids problems, and it is also capable of analyzing the transient heat conduction in multilayer FGMs under convective boundary conditions.

## Acknowledgement

The financial support from the Fundamental Research Funds for the Central Universities HEUCFP201711 is gratefully acknowledged.

## References

[1] Koizumi M., Niino M., Overview of FGM research in Japan. Mrs Bulletin, 1995, 20: 19–21.

[2] Chan S.H., Khor K.A., The effect of thermal barrier coated piston crown on engine characteristics. Journal of Materials Engineering and Performance, 2000, 9: 103–109.

[3] Buyukkaya E., Thermal analysis of functionally graded coating alsi alloy and steel pistons. Surface and Coatings Technology, 2008, 202: 3856–3865.

[4] Zhao B., Thermal stress analysis of ceramic-coated diesel engine pistons based on the wavelet finite-element

method. Journal of Engineering Mechanics, 2012, 138(1): 143–149.

[5] Thieme M., Wieters K.P., Bergner F., Titanium sintering for preparation of a porous functionally graded material destined for orthopaedic implants. Journal of Materials Science Materials in Medicine, 2001, 12(3): 225–231.

[6] Suk M.J., Choi S.I., Kim J.S., Kim Y. Do, Kwon Y.S., Fabrication of a porous material with a porosity gradient by a pulsed electric current sintering process. Metals and Materials International, 2003, 9(6): 599–603.

[7] Hideki S., Katsumi K., Hitoshi O., Application feasibility of permittivity graded fgm (functionally graded materials) for gas insulated equipment. IEEJ Transactions on Power and Energy, 2005, 125(7): 695–700.

[8] Kato K., Kurimoto M., Shumiya H., Application of functionally graded material for solid insulator in gaseous insulation system. IEEE Transactions on Dielectrics and Electrical Insulation, 2006, 13(2): 362–372.

[9] Ootao Y., Tanigawa Y., Fukuda T., Axisymmetric transient thermal stress analysis of a multilayered composite hollow cylinder. Journal of Thermal Stresses, 1991, 14(2): 201–213.

[10] Ootao Y., Akai T., Tanigawa Y., Three-dimensional transient thermal stress analysis of a nonhomogeneous hollow circular cylinder due to a moving heat source in the axial direction. Journal of Thermal Stresses, 1995, 18(5): 497–512.

[11] Tanigawa, Ootao Y., Yoshinobu, Three-dimensional transient thermal stresses of functionally graded rectangular plate due to partial heating. Journal of Thermal Stresses, 1999, 22(1): 35–55.

[12] Vel S., Batra R., C,. Exact solution for thermoelastic deformations of functionally graded thick rectangular plate. Aiaa Journal, 2012, 40(7): 1421–1433.

[13] Lutz M.P., Zimmerman R.W., Thermal stresses and effective thermal expansion coefficient of a functionally gradient sphere. Journal of Thermal Stresses, 1996, 19(1): 39–54.

[14] Zhou Y.T., Lee K.Y., Yu D.H., Transient heat conduction in a functionally graded strip in contact with well stirred fluid with an outside heat source. International Journal of Heat and Mass Transfer, 2011, 54(25-26): 5438–5443.

[15] Sladek J., Sladek V., Krivacek J., Local BIEM for transient heat conduction analysis in 3-D axisymmetric functionally graded solids. Computational Mechanics, 2003, 32(3): 169–176.

[16] Sutradhar A., Paulino G.H., Gray L.J., Transient heat conduction in homogeneous and non-homogeneous materials by the Laplace transform Galerkin boundary element method. Engineering Analysis with Boundary Elements, 2002, 26(2): 119–132.

[17] Sutradhar A., Paulino G.H., Gray L.J., On hypersingular surface integrals in the symmetric Galerkin boundary element method: application to heat conduction in exponentially graded materials. International Journal for Numerical Methods in Engineering, 2005, 62(1): 122–157.

[18] Wang H., Qin Q. H., Kang Y.L., A meshless model for transient heat conduction in functionally graded materials. Computational Mechanics, 2006, 38(1): 51–60.

[19] Wang B.L., Mai Y.W., Zhang X.H., Thermal shock resistance of functionally graded materials. Acta Materialia, 2004, 52(17): 4961–4972.

[20] Yu Y., Cui J., Han F., The statistical second-order two-scale analysis method for heat conduction performances of the composite structure with inconsistent random distribution. Computational Materials Science, 2009, 46(1): 0–161.

[21] Aboudi J., Pindera M.J., Arnold S.M., Higher-order theory for functionally graded materials. Composites Part B Engineering, 1999, 30(8): 777–832.

[22] Bansal Y., Pindera M.J., Efficient reformulation of the thermoelastic higher-order theory for functionally graded materials. Journal of Thermal Stresses, 2003, 26(11-12): 1055–1092.

[23] Zhong Y., Bansal Y., Pindera M.J., Efficient reformulation of the thermal high reorder theory for fgms with locally variable thermal conductivity. International Journal of Computational Engineering Science, 2004, 5: 795–831.

[24] Bansal Y., Finite-volume direct averaging micromechanics of heterogeneous media. Engineering and Applied Science University of Virginia, VA; 2005. Virginia, USA.

[25] Gong J.F., Xuan L.K., Ming P.J., Application of the staggered cell-vertex finite volume method to thermoelastic analysis in heterogeneous materials. Journal of Thermal Stresses, 2014, 37(4): 506–531.

[26] Gong J., Xuan L., Ming P., An unstructured finite-volume method for transient heat conduction analysis of multilayer functionally graded materials with mixed grids. Numerical Heat Transfer, Part B: Fundamentals, 2013, 63(3): 222–247.

[27] Charoensuk J., Vessakosol P., A high order control volume finite element procedure for transient heat conduction analysis of functionally graded materials. Heat and Mass Transfer, 2010, 46(11–12): 1261–1276.

[28] Wang X.C., Finite element method. Tsinghua University Press, Beijing, 2003.

[29] Liu Y., Zhang X., Lu M.W., A meshless method based on least-squares approach for steady- and unsteady-state heat conduction problems. Numerical Heat Transfer, Part

B, 2005, 47(3): 257–275.

[30] Ching H.K., Yen S.C., Transient thermoelastic deformations of 2-D functionally graded beams under nonuniformly convective heat supply. Composite Structures, 2006, 73(4): 381–393.

[31] Sutradhar A., Paulino G.H., The simple boundary element method for transient heat conduction in functionally graded materials. Computer Methods in Applied Mechanics and Engineering, 2004, 193(42-44): 4511–4539.

[32] Pisani S.R., Rencis J.J., Investigating CURVIC coupling behavior by utilizing two- and three-dimensional boundary and finite element methods. Engineering Analysis with Boundary Elements, 2000, 24(3): 271–275.

## Appendix 1. Details of the way to deal with 9-node quadrilateral grid

The shape functions, their derivatives and numerical integration method in 6-node triangular grid have been reported in Ref. [22]. Here we only list details of the way to deal with 9-node quadrilateral grid. Fig. 27 shows the global coordinate and local coordinate of any 9-node quadrilateral grid. The shape functions and their derivatives with respect to $\xi$ and $\eta$ are summarized in table 6.

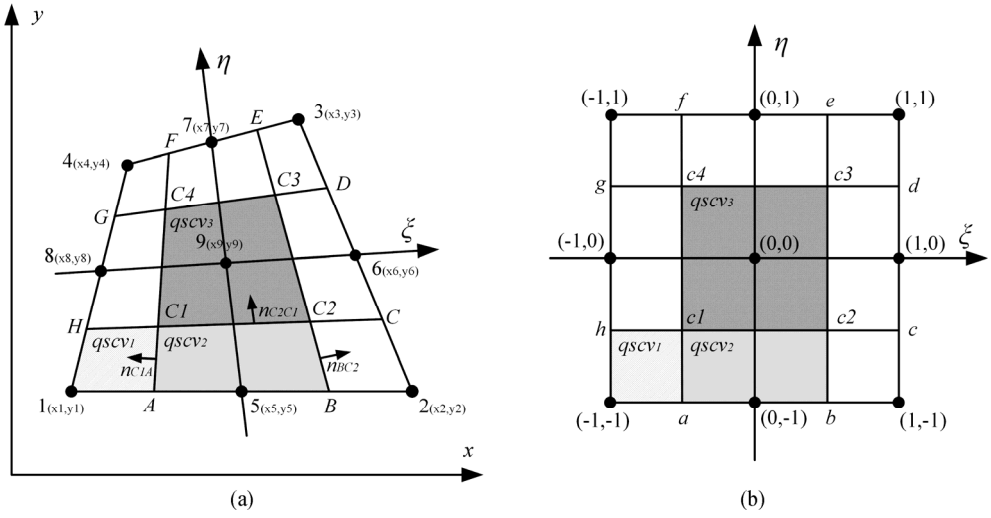


**Fig. 27** Any 9-node quadrilateral grid: Global coordinate (a) and local coordinate (b)

**Table 6** The shape functions and their derivatives with respect to $\xi$ and $\eta$ for 9-node quadrilateral grid

| $N_i$ | $\frac{\partial N_i}{\partial \xi}$ | $\frac{\partial N_i}{\partial \eta}$ |
|---|---|---|
| $\xi\eta(1-\xi)(1-\eta)/4$ | $\eta(2\xi-1)(\eta-1)/4$ | $\xi(2\eta-1)(\xi-1)/4$ |
| $-\xi\eta(1+\xi)(1-\eta)/4$ | $\eta(2\xi+1)(\eta-1)/4$ | $\xi(2\eta-1)(\xi+1)/4$ |
| $\xi\eta(1+\xi)(1+\eta)/4$ | $\eta(2\xi+1)(\eta+1)/4$ | $\xi(2\eta+1)(\xi+1)/4$ |
| $-\xi\eta(1-\xi)(1+\eta)/4$ | $\eta(2\xi-1)(\eta+1)/4$ | $\xi(2\eta+1)(\xi-1)/4$ |
| $(-\xi)(1-\eta)(1-\xi^2)/2$ | $-\xi\eta(\eta-1)$ | $-(\xi^2-1)(2\eta-1)/2$ |
| $\xi(1+\xi)(1-\eta^2)/2$ | $-(2\xi+1)(\eta^2-1)/2$ | $-\xi\eta(\xi+1)$ |
| $\xi(1+\eta)(1-\xi^2)/2$ | $-\xi\eta(\eta+1)$ | $-(\xi^2-1)(2\eta+1)/2$ |
| $(-\xi)(1-\xi)(1-\eta^2)/2$ | $-(2\xi-1)(\eta^2-1)/2$ | $-\xi\eta(\xi-1)$ |
| $(1-\xi^2)(1-\eta^2)$ | $2\xi(\eta^2-1)$ | $2\eta(\xi^2-1)$ |

The derivatives of shape functions with respect to local coordinate can be expressed as

$$\begin{Bmatrix} \dfrac{\partial N_i}{\partial \xi} \\ \dfrac{\partial N_i}{\partial \eta} \end{Bmatrix} = \begin{bmatrix} \dfrac{\partial x}{\partial \xi} & \dfrac{\partial y}{\partial \xi} \\ \dfrac{\partial x}{\partial \eta} & \dfrac{\partial y}{\partial \eta} \end{bmatrix} \begin{Bmatrix} \dfrac{\partial N_i}{\partial x} \\ \dfrac{\partial N_i}{\partial y} \end{Bmatrix} = [J] \begin{Bmatrix} \dfrac{\partial N_i}{\partial x} \\ \dfrac{\partial N_i}{\partial y} \end{Bmatrix} \tag{34}$$

where [$J$] is the Jacobian matrix. The components of the Jacobian matrix with respect to global coordinate can be expressed as

$$\begin{aligned} \frac{\partial x}{\partial \xi} &= \sum_{i=1}^{n} \frac{\partial N_i}{\partial \xi} x_i, \quad \frac{\partial y}{\partial \xi} = \sum_{i=1}^{n} \frac{\partial N_i}{\partial \xi} y_i \\ \frac{\partial x}{\partial \eta} &= \sum_{i=1}^{n} \frac{\partial N_i}{\partial \eta} x_i, \quad \frac{\partial y}{\partial \eta} = \sum_{i=1}^{n} \frac{\partial N_i}{\partial \eta} y_i \end{aligned} \tag{35}$$

where $n$ is the number of nodes making up a mesh element, for 9-node quadrilateral grid, $n$=9.

By mapping the derivatives of shape functions back to global coordinate, the required derivatives $\dfrac{\partial N_i}{\partial x}$ and $\dfrac{\partial N_i}{\partial y}$ can be obtained

$$\begin{Bmatrix} \dfrac{\partial N_i}{\partial x} \\ \dfrac{\partial N_i}{\partial y} \end{Bmatrix} = [J]^{-1} \begin{Bmatrix} \dfrac{\partial N_i}{\partial \xi} \\ \dfrac{\partial N_i}{\partial \eta} \end{Bmatrix} \tag{36}$$

There are nine sub-control volumes within each 9-node quadrilateral grid shown as Fig. 28. The integral for the partial derivatives of shape functions over faces is calculated by the midpoint rule since it gives high accuracy with little effort expended. Take node 1 for example, $\int_l k_\alpha \dfrac{\partial T}{\partial \alpha} n_\alpha dl$ can be expressed as:

$$\begin{aligned} \int_{a-c1-h} k_\alpha \frac{\partial T}{\partial \alpha} n_\alpha dl = {} & \Delta y_{ac1} \sum_{j=1}^{9} T_j \left( k_x \frac{\partial N_j}{\partial x} \right)_{ac1} + \Delta y_{c1h} \sum_{j=1}^{9} T_j \left( k_x \frac{\partial N_j}{\partial x} \right)_{c1h} \\ & - \Delta x_{ac1} \sum_{j=1}^{9} T_j \left( k_y \frac{\partial N_j}{\partial y} \right)_{ac1} - \Delta x_{c1h} \sum_{j=1}^{9} T_j \left( k_y \frac{\partial N_j}{\partial y} \right)_{c1h} \end{aligned} \tag{37}$$

where $\Delta y_{mn}=y_m-y_n$ and $\Delta x_{mn}=x_m-x_n$.

Fig. 28 shows the integration points on the faces surrounding node $i$ within 9-node quadrilateral grid. The locations of integration points are summarized in Table 7.

**Table 7** Integration points for 9-node quadrilateral grid

| Face\node | 1 | 2 | 3 | 4 | 5 |
|---|---|---|---|---|---|
| $S_1$ | (−1/2, −3/4) | (3/4, −1/2) | (1/2,3/4) | (−3/4,1/2) | (1/2, −3/4) |
| $S_2$ | (−3/4, −1/2) | (1/2, −3/4) | (3/4,1/2) | (−1/2,3/4) | (0, −1/2) |
| $S_3$ | - | - | - | - | (−1/2, −3/4) |
| $S_4$ | - | - | - | - | - |
| Face\node | 6 | 7 | 8 | 9 | |
| $S_1$ | (3/4,1/2) | (−1/2,3/4) | (−3/4, −1/2) | (0, −1/2) | |
| $S_2$ | (1/2,0) | (0,1/2) | (−1/2,0) | (1/2,0) | |
| $S_3$ | (3/4, −1/2) | (1/2,3/4) | (−3/4,1/2) | (0,1/2) | |
| $S_4$ | - | - | - | (−1/2,0) | |

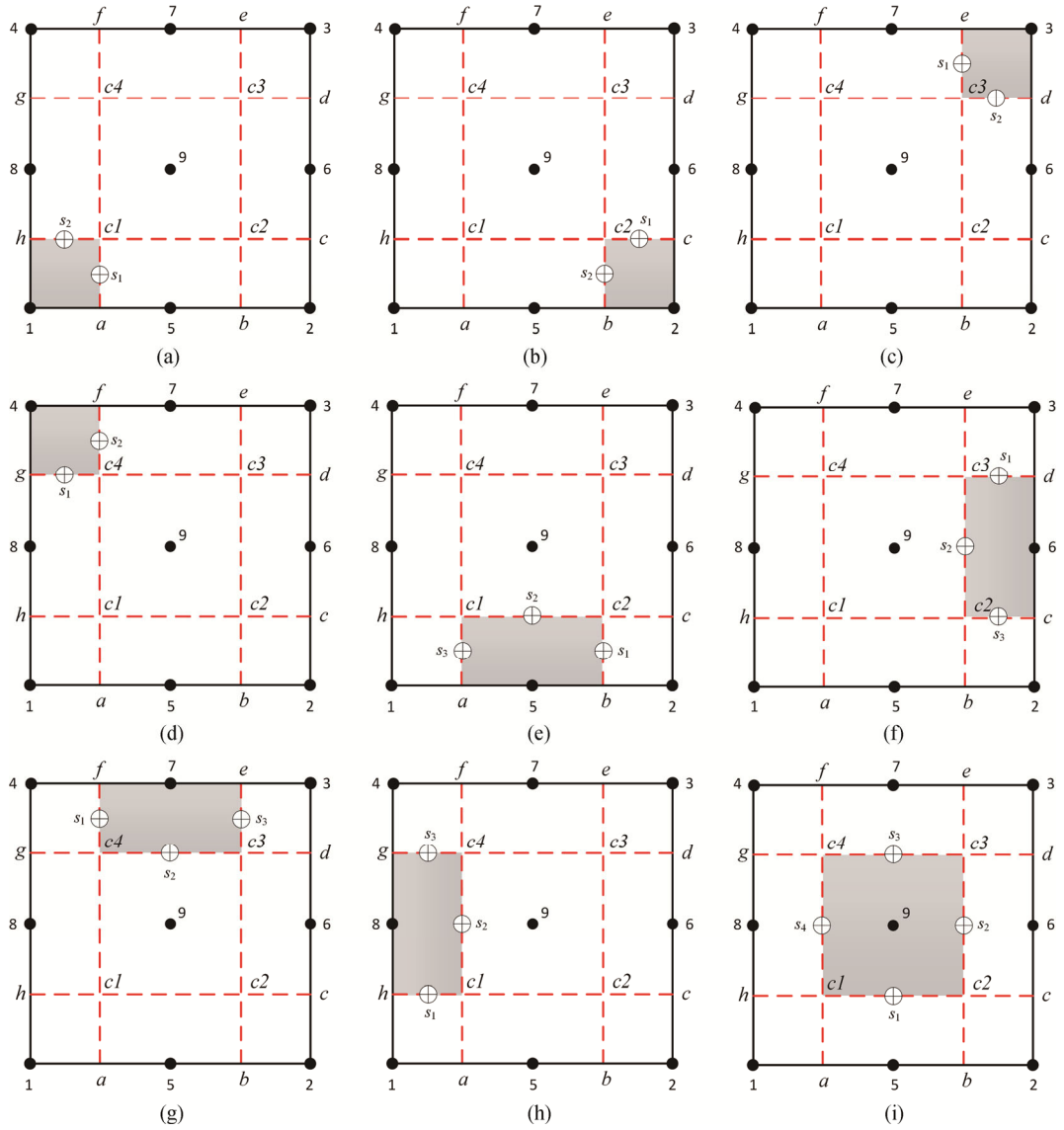


**Fig. 28** Integration points along the faces surrounding (a) node 1, (b) node 2, (c) node 3, (d) node 4, (e) node 5, (f) node 6, (g) node 7, (h) node 8 and (i) node 9